



# Size-dependent He-irradiated tolerance and plastic deformation of crystalline/amorphous Cu/Cu–Zr nanolaminates

J.Y. Zhang, Y.Q. Wang, X.Q. Liang, F.L. Zeng, G. Liu\* and J. Sun\*

State Key Laboratory for Mechanical Behavior of Materials, Xi'an Jiaotong University, Xi'an 710049, People's Republic of China

Received 12 December 2014; revised 17 March 2015; accepted 31 March 2015

Available online 14 April 2015

**Abstract**—Nanoindentation methodology was used to measure the hardness, strain rate sensitivity (SRS) and activation volume of Cu/Cu–Zr crystalline/amorphous nanolaminates (C/ANLs) with layer thickness ( $h$ ) spanning from 2.5 to 150 nm before and after He ion-implantation at room temperature. It is interestingly to uncover that the ion radiation-induced devitrification (RID) occurs in the glassy Cu–Zr nanolayers, in which the nanocrystallites transit from the  $\text{Cu}_{10}\text{Zr}_7$  intermetallics at large  $h$  to the fcc Cu–Zr solid solution at small  $h$ . Compared with the as-deposited Cu/Cu–Zr C/ANLs associated with monotonic increase in hardness and SRS (or a monotonic decrease in activation volume) with reducing  $h$ , the irradiated Cu/Cu–Zr manifested enhanced hardness in the form of two hardness plateau and an unexpected non-monotonic variation in SRS (similarly in activation volume). It was clearly unveiled that the SRS of irradiated Cu/Cu–Zr firstly decreased with reducing  $h$  down to a critical size of  $\sim 50$  nm and subsequently increased with further reducing  $h$  to  $\sim 10$  nm, below which a SRS  $m$  plateau emerges (The activation volume of irradiated Cu/Cu–Zr had exactly an opposite variation). These phenomena are rationalized by considering a competition between dislocation-interface and dislocation-bubble interactions. A thermally activated model based on the depinning process of bowed-out dislocations pinned by obstacles was employed to quantitatively account for the variation of SRS with  $h$  in Cu/Cu–Zr C/ANLs before and after radiation. Our findings not only provide fundamental understanding of the effects of radiation-induced defects on plastic characteristics of C/ANLs, but also offer guidance for their microstructure sensitive design for performance optimization at extremes.

© 2015 Acta Materialia Inc. Published by Elsevier Ltd. All rights reserved.

**Keywords:** Crystalline/amorphous nanolaminates; Crystallization; Deformation mechanisms; Radiation tolerance; Size effects

## 1. Introduction

It is well accepted that heavy ion radiation of metallic crystals can cause dramatic variations of microstructure, including amorphization or phase change [1–4]. Previous investigation [5–7] on helium (He)-radiation has verified that, due to nuclear collisions lighter He ions can induce a higher ratio of point defects (e.g. vacancies and interstitials) produced relative to defect clusters (e.g. He bubbles) in metallic crystals. This in turn remarkably degrades the performance of structural materials in advanced fission/fusion reactors, which must be significantly improved to extend the reliability and efficiency [8–10]. Because of the detrimental effects of radiation-induced defects and He accumulation from transmutation reactions on materials mechanical properties, radiation environments pose a great challenge for materials scientists in terms of choosing and designing materials that resist radiation damage while maintaining high strength and toughness.

It has long been known that grain boundaries and heterophase interfaces are sinks for radiation-induced point defects and traps for He [1,7,11–13]. Therefore, a universal strategy for developing materials that withstand radiation under harsh conditions has long focused on creating microstructures with high densities of sinks or traps for point defects. Recently, active research on response metallic crystalline/crystalline interfaces (CCIs) under radiation has been studied in numerous metallic crystalline/crystalline nanolaminates (C/CNLs) with fcc/bcc interfaces (e.g. Cu/Nb [14], Cu/V [15], Al/Nb [16] and Ag/V [17]), fcc/fcc interfaces (e.g. Cu/Ni [18], Cu/Co [19], Ag/Ni [20]) and bcc/bcc interfaces (e.g. Fe/W [21]). These C/CNLs that contain a large volume fraction of interfaces have manifested intriguing characteristics compared to bulk metals under radiation, including an order of magnitude increase in strength, several orders of magnitude higher He solid solubility, dramatic reduction of bubble density and much lower radiation hardening [13–20]. Specifically, it is the competition between the internal length, such as layer thickness ( $h$ ) in NLs, and the spacing ( $l$ ) or size ( $d$ ) of radiation-induced defects that controls the strength of ion-irradiated nanostructured materials. Correspondingly, some phenomenological hardening models have been proposed to

\* Corresponding authors. Tel.: +86 (0)2982667143; fax: +86 (0)2982663453; e-mail addresses: [lgsammer@mail.xjtu.edu.cn](mailto:lgsammer@mail.xjtu.edu.cn); [junsun@mail.xjtu.edu.cn](mailto:junsun@mail.xjtu.edu.cn)

explain the size  $h$ -dependent radiation (e.g. He bubbles) hardening in NLs in three regions at different lengths [17]: (i) when  $h$  is smaller than bubble spacing, the interface crossing mechanism dominates in NLs without bubble hardening; (ii) when  $h$  falls into the regime of confined layer slip (CLS) model, the bubble hardening model have been established according to Friedel–Kroupa–Hirsch model; and (iii) when  $h$  is much larger, a bulk-like bubble hardening behavior is observed in NLs.

Unlike the well-defined long-range order that characterizes crystalline metals, the atomic arrangements in metallic glasses with amorphous nature exhibit the short-to-medium-range ordering features [22,23]. Such significant difference in their internal features suggests that the atomic-scale radiation response mechanisms of metallic glasses are qualitatively different from those found in crystalline alloys [24,25]. Previously studies have uncovered that because their internal amorphous structure provides sufficient room to accommodate the He bubbles or other defects, the metallic glasses, in particular for the Zr-based metallic glasses with a greater glass forming ability, exhibited better radiation tolerance than the metallic crystals [25–27], though the phenomenon of (electron/ion) radiation-induced devitrification (RID) has been observed in some glassy materials [25,26]. Specifically, Nagase and Umakoshi [26,27] clearly demonstrated that, due to irradiation knock-on effect rather than temperature increase, electron irradiation can induce, even accelerate nanocrystallization of an amorphous phase in metallic glasses at  $\sim 103$  K, in which devitrification is difficult to realize by thermal annealing. They further suggested that two premises should be satisfied simultaneously to achieve RID [26,27], i.e., (i) the atomic diffusion promoted by irradiation in an amorphous phase and (ii) the phase stability of crystalline phases against irradiation. Compared with the metallic C/CNLs, recent findings have clearly demonstrated that the combination of crystalline nanolayers with amorphous nanolayers in the form of metallic crystalline/amorphous NLs (C/ANLs) manifest more superior mechanical properties, such as large tensile ductility [28] and self-toughening capability [29,30], all of which are closely correlated with the crystalline/amorphous interfaces (CAIs) as well as the unique properties/structures of glassy nanolayers [29–32]. The CAIs exhibit unique inelastic shear/slip transfer characteristics while avoiding extreme stress concentrations, fundamentally different from those of CCIs associated with strain or geometric incompatibilities [31], as verified by both atomistic simulations [28,32] and experiments [34,35]. The unique interfacial structures/characteristics of CAIs have stimulated increasing interest in the mechanical properties and their underlying mechanisms of C/ANLs possessing tunable length scales before and after ion-radiation.

In this paper, Cu/Cu–Zr C/ANLs with CAIs were selected as the studied materials. Plastic deformation behavior of Cu/Cu–Zr was comparatively investigated before and after He-radiation. The size  $h$ -dependent radiation hardening and  $h$ -dependent RID were experimentally uncovered. Based on microstructural analyses on interface and radiation-induced bubbles, possible deformation mechanisms contributing to mechanical properties are discussed and dislocation-based models are used to quantitatively describe the size-dependent deformation behavior in these He-irradiated C/ANLs.

## 2. Experimental procedures

### 2.1. Sample preparation and implantation experiments

Cu (99.995%) and Zr (99.99%) targets were used to deposit Cu/Cu<sub>60</sub>Zr<sub>40</sub> C/ANLs on HF-etched Si (100) substrates by direct current (DC) magnetron sputtering at room temperature. The chamber was evacuated to a base pressure of  $\sim 6.0 \times 10^{-8}$  Torr, and  $1.0\text{--}2.5 \times 10^{-3}$  Torr of Ar was maintained during the deposition process. The substrate was neither heated nor cooled during the deposition process. The constituent layers in Cu/Cu–Zr C/ANLs have equal thickness of  $h$ , and a wide range of  $h$  ranging from 2.5 to 150 nm was designed to disclose the intrinsic size effect. The total thickness of the Cu/Cu–Zr C/ANLs was  $\sim 2$   $\mu\text{m}$  for  $h < 100$  nm and  $\sim 3.6$   $\mu\text{m}$  for  $h \geq 100$  nm. The Cu seed layer with 100 nm thickness is deposited directly on the Si (100) substrates, and the cap layer of the Cu/Cu–Zr C/ANLs is Cu. More details about the preparation and microstructure features of these C/ANLs can be found in our previous work [33,34], and will not be presented here. For comparison reasons, the single layer Cu film with grain size ( $d$ ) of  $\sim 180$  nm and monolithic Cu<sub>60</sub>Zr<sub>40</sub> amorphous thin films are also prepared on Si (100) substrates. The implantation experiment was performed at room temperature using a He ion energy of 40 keV associated with the ion flux rate of  $\sim 1 \times 10^{-4}$  dpa·s<sup>-1</sup> to a total fluence of  $1 \times 10^{17}$  ions·cm<sup>-2</sup> at a constant beam current of  $\sim 2.5$   $\mu\text{A}$ . During radiation the base pressure was maintained at  $1 \times 10^{-4}$  Pa. He concentration vs. penetration depth was simulated by SRIM software [17,35], indicating the maximum implantation depth is  $\sim 350$  nm and the maximum He concentration is reached at the depth of  $\sim 150\text{--}200$  nm for Cu/Cu–Zr C/ANLs and constituents (Cu and Cu–Zr) thin films (see Figs. 4 and 6).

### 2.2. Microstructure characterizations

X-ray diffraction (XRD) was performed at room temperature using an improved Rigaku D/max-ray diffractometer with Cu K $\alpha$  radiation and a graphite monochromator to determine the crystallographic texture. High resolution transmission electron microscopy (HRTEM) was performed on a JEOL-2010F microscope operated at 200 kV, with Fischione ultra-high resolution high-angle annular dark field detector (0.23 nm resolution in STEM image mode) to observe the internal features, such as grain sizes and He bubble sizes and distributions. The convergent beam electron diffraction (CBED) technique, which can reach an accuracy of  $\sim 5\%$  in determining foil thickness [19] was employed to measure the average TEM foil thickness. The thickness of the TEM foils was measured to be  $\sim 150 \pm 30$  nm throughout the irradiated regions in multilayers. More details about CBED method can be referred to Ref. [36]. Energy dispersive X-ray (EDX) analyses were carried out to identify the elemental composition and the interface integrity of the specimens by Oxford instruments EDX detector with a spatial resolution of  $\sim 1$  nm for chemical analysis.

### 2.3. Nanoindentation test

The mechanical properties of both Cu/Cu<sub>60</sub>Zr<sub>40</sub> C/ANLs and Cu thin films before and radiation studied here

were measured using an Agilent G200 nanoindenter system with standard Berkovich tips under the displacement controlled mode (corresponding to the constant loading strain rate ( $\dot{\epsilon}$ ) of  $0.05 \text{ s}^{-1}$ ). The nanoindentation test was performed at room temperature, following the Oliver–Pharr method [37]. The indentation depth was set at  $\sim 200 \text{ nm}$  within the range of implanted He ions of  $\sim 350 \text{ nm}$ , guaranteeing that the He bubbles were involved sufficiently during the deformation while avoiding the effect of Si substrate. Here we measured the SRS index ( $m$ ) and activation volume ( $V^*$ ) by using nanoindentation creep method with the holding time of  $100 \text{ s}$ , details of this method can be referred to Ref. [38], which is also adapted by others [39–41]. Note that only the data in the steady state creep stage (where the effect of strain hardening was minimized) were used to calculate the strain rate sensitivity, in order to reduce the data dispersity. Great efforts were devoted to calibrate the thermal drift, following our previous work [38].

An example of the calculation of SRS  $m$  for  $h = 20 \text{ nm}$  Cu/Cu–Zr C/ANLs after radiation is shown in Fig. 1. The SRS  $m$  is defined as the slope of the double logarithmic plot of hardness ( $H$ ) vs. strain rate ( $\dot{\epsilon}$ ) [42]

$$m = \frac{\partial \ln(H)}{\partial \ln(\dot{\epsilon})}, \quad (1)$$

While the activation volume can be expressed by the following formula

$$V^* = \frac{2.7 \times \sqrt{3} kT}{Hm}, \quad (2)$$

where  $k$  is the Boltzmann constant and  $T$  is the temperature. A minimum of 15 indents separated from each other by at least  $50 \mu\text{m}$  were performed on each sample to obtain an average hardness ( $H$ ), i.e.,  $H = 2.7 \times \sigma$  ( $\sigma$  is strength).

### 3. Results

#### 3.1. Microstructural features of the Cu/Cu–Zr C/ANLs before and after irradiation

High-angle XRD patterns shown in Fig. 2 reveal that all the Cu/Cu<sub>60</sub>Zr<sub>40</sub> C/ANLs (before and after radiation) show a strong Cu (111) texture that broadens with decreasing  $h$  and quite weak peak intensity of glassy phase, while the Cu thin films exhibit a strong Cu (111)-peak (Note that the Cu (200)-peak stems from the highly textured Cu seed layer, which sustains constant intensity and can serve as a reference to Cu (111)-peak.). No diffraction peaks of He and other crystalline phases are observed in irradiated Cu/Cu<sub>60</sub>Zr<sub>40</sub> C/ANLs and constituents (Cu and Cu–Zr) thin films. It is striking to find that, compared with the unstressed state of unirradiated C/ANLs (or those of large  $h \geq 10 \text{ nm}$  irradiated samples), the diffraction peak of Cu (111) shifts toward to low diffraction angle ( $\sim 42.6^\circ$ ) and the peak intensity increase occurs in  $h < 10 \text{ nm}$  irradiated C/ANLs. It is suggested that there is a change in the lattice parameter of constituent(s) layers, which likely renders the formation of new interfacial structure (discussed below).

The typical cross-sectional TEM image of as-deposited Cu/Cu–Zr C/ANLs with  $h = 5, 10$  and  $50 \text{ nm}$  is displayed in Fig. 3a–c, respectively, showing the chemically modulated layer structure and distinguishable CAIs. The corresponding selected area diffraction pattern (SADP) shows that all the Cu/Cu–Zr C/ANLs have a strong Cu (111) texture and fully amorphous nature of glassy layers, consistent with the XRD results. The size of columnar grains in the Cu layers scales with the layer thickness, and some growth nanotwins are observed in the Cu layers. More details about the internal features of the Cu/Cu–Zr C/ANLs can be found in our previous work [48,56], and will not be discussed here. The cross-sectional TEM image of as-deposited Cu thin film as well as its corresponding

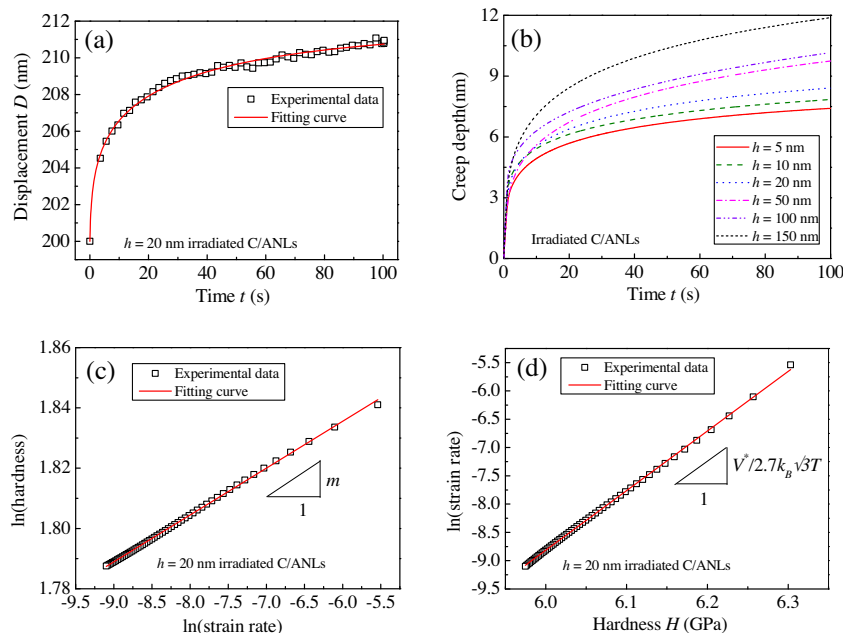


**Fig. 1.** (a) An example of experimental data and fitting creep curve of the Cu/Cu–Zr C/ANLs with  $h = 20 \text{ nm}$  after radiation. (b) Creep responses for He-irradiated C/ANLs with different  $h$ . Example of the experimental method to determine  $m$  (c) and  $V^*$  (d).

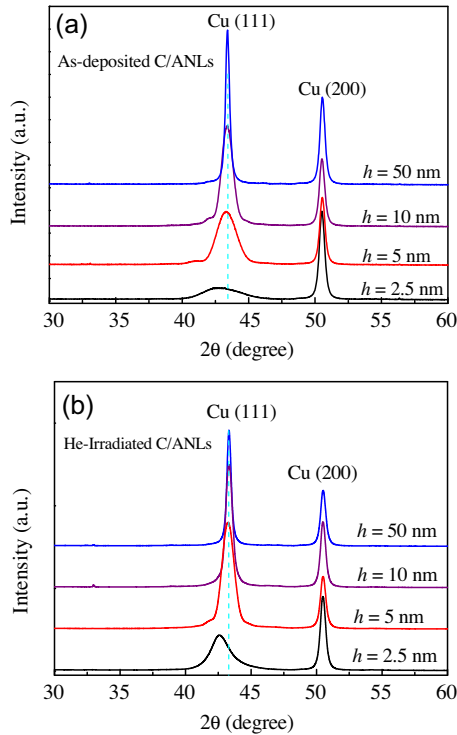


**Fig. 2.** XRD patterns for Cu/Cu–Zr C/ANLs with different  $h$  before (a) and after (b) radiation.

SADP are displayed in Fig. 3d, from which one can see the average grain size ( $d$ ) is of  $\sim 180 \pm 30$  nm.

The typical cross-sectional TEM micrographs under-focus of 500 nm of irradiated Cu/Cu–Zr samples with

$h = 2.5, 5, 10$  and  $50$  nm in the peak-damage region are shown in Fig. 4. Interestingly, lots of nanocrystallites caused by RID are observed in glassy Cu–Zr layers, implying the meta-stable nature of the amorphous phase. Moreover, the phenomenon of RID exhibits a non-monotonic size dependent behavior, i.e., a minimum fraction of crystalline phase of unit area in glassy layers emerges in the  $h = 10$  nm irradiated Cu/Cu–Zr C/ANLs, as shown in Fig. 5. In other words, the fraction of crystallites first decreases with decreasing  $h$  to  $10$  nm and then in turn increases with further decreasing  $h$ . Specifically, most of the nanocrystallites in large  $h \geq 10$  nm Cu/Cu–Zr samples is  $\text{Cu}_{10}\text{Zr}_7$  with sizes ranging from  $\sim 2$ – $15$  nm (see Fig. 4f). In contrast, the glassy nanolayers are crystallized to a great extent in small  $h < 10$  nm samples after radiation and the crystalline phase seems to be the fcc Cu–Zr “solid solution” (see Fig. 4a), as is supported by XRD patterns. The (localized) coherent interface between Cu and fcc Cu–Zr layer is formed, as verified by the Burgers circuits in Fig. 4a. The SADPs also indicate a strong Cu  $\{111\}$  texture in Cu/Cu–Zr C/ANLs, which was unaffected by ion-implantation. The SRIM prediction as the inset in Fig. 4g shows the He concentration as a function of implantation depth in  $h = 50$  nm Cu/Cu–Zr C/ANLs. It appears that the peak He concentration of  $\sim 7.0$  at.% is reached at a depth of  $\sim 150$ – $200$  nm. Similar results, such as the He concentration and crystallographic orientation of grains are observed in Cu thin films, see Fig. 6.

Since the initial plastic deformation of C/ANLs is dominated by the soft Cu layers [34,44,45], careful microstructure examinations have been performed in all the irradiated samples at an identical implantation depth of  $\sim 150$ – $200$  nm to characterize the bubble distribution in Cu layers and to examine the size-dependent radiation tolerance of C/

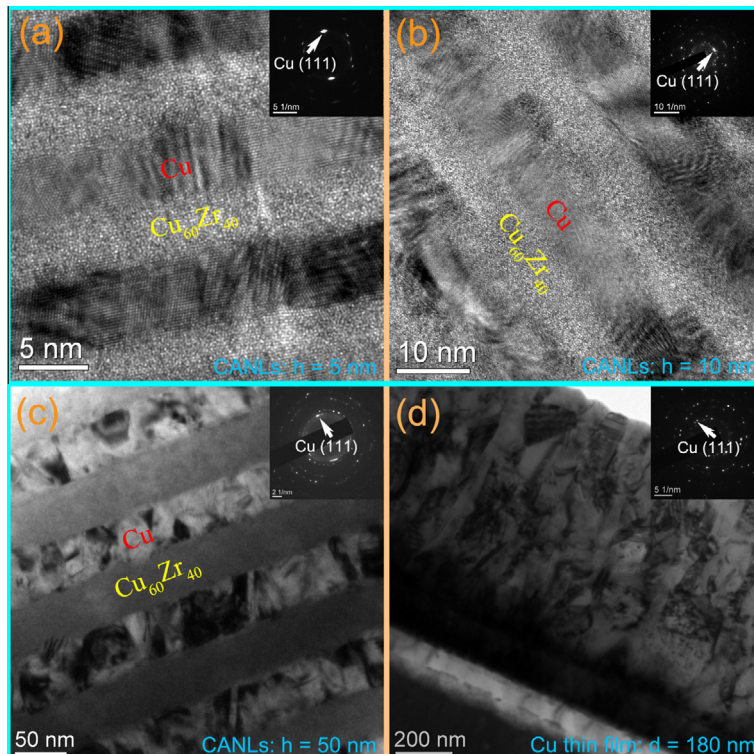


**Fig. 3.** (a) Bright field cross-sectional TEM micrograph showing the microstructure of the as-deposited Cu/Cu–Zr C/ANLs with  $h = 5$  nm (a),  $h = 10$  nm (b),  $h = 50$  nm (c) and as-deposited Cu thin film (d). Insets are the corresponding selected area diffraction pattern (SADP).

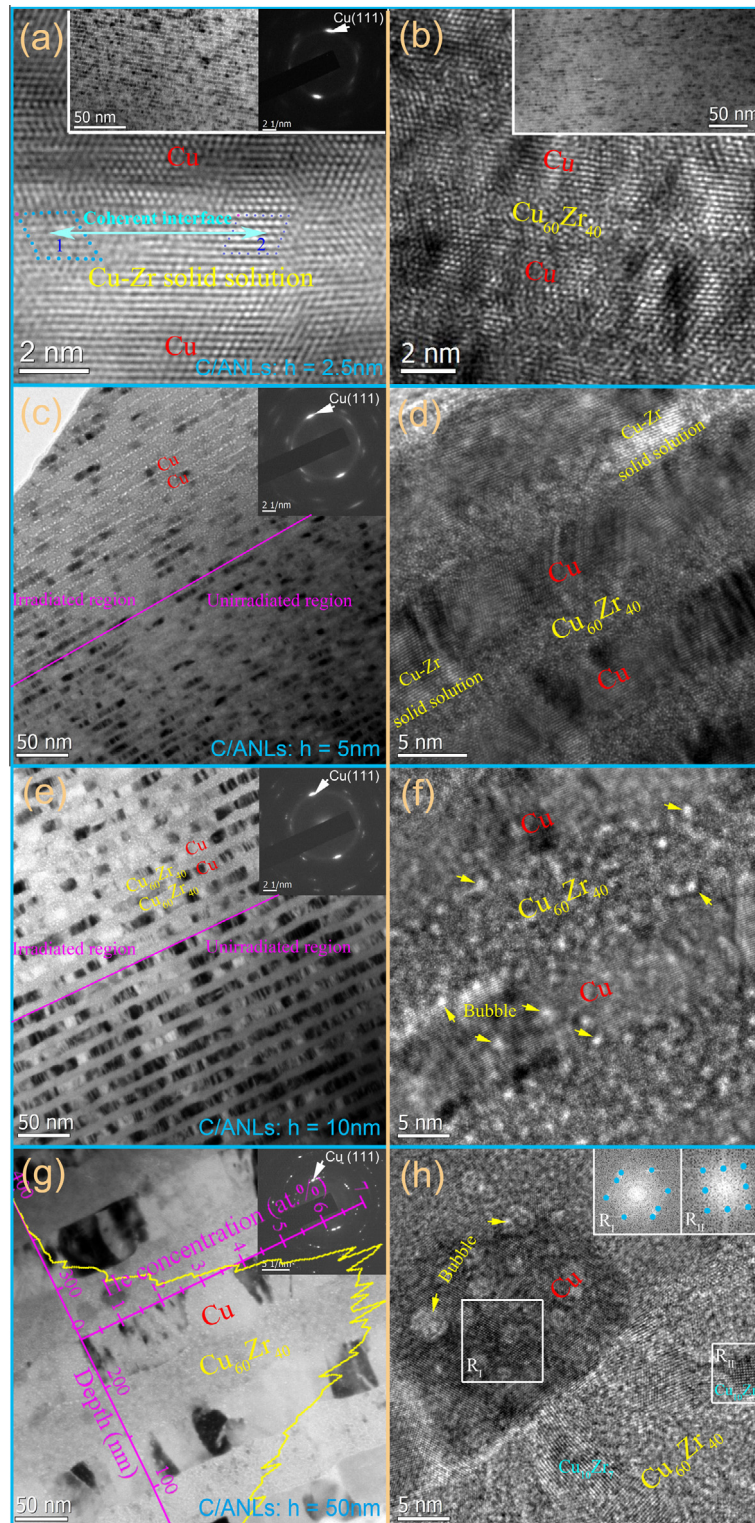


**Fig. 4.** Bright field cross-sectional TEM images for He-irradiated Cu/Cu-Zr C/ANLs with  $h = 2.5$  nm (a),  $h = 5$  nm (c, d),  $h = 10$  nm (e, f) and  $h = 50$  nm (g, h), showing nanolayered microstructure and crystallization of Cu-Zr amorphous layers. The corresponding selected area diffraction patterns (SADPs) show no change in crystallographic orientation. (b) is high-resolution TEM image and low magnified image (inset) for the as-deposited C/ANLs with  $h = 2.5$  nm, showing modulated layered structure and distinguishable CAIs. Two Burgers circuit are labeled 1 and 2 in (a), respectively, to determine the Burgers vector of misfit dislocations, verifying the fully (localized) coherent interface between Cu and Cu-Zr solid solution layers. Superimposed on image (g) is the He concentration vs. Depth profile simulated by SRIM. Insets in (h) is respectively the fast Fourier transform (FFT) pattern of region-I (R-I, Cu) and region-II (R-II, Cu<sub>10</sub>Zr<sub>7</sub>), showing different crystalline orientations. Some bubbles within the Cu layers are representatively marked by arrows. All the observations for the irradiated samples are in the conditions of under-focus of 500 nm ( $\Delta f = -500$  nm).

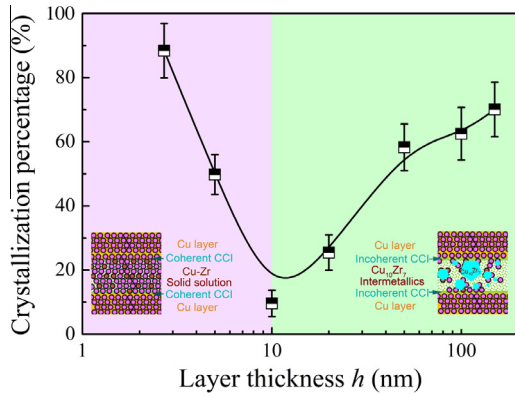


**Fig. 5.** Layer thickness  $h$ -dependent crystallization (or RID) mechanism map, divided by a critical layer thickness of  $\sim 10$  nm, below this critical size RID leads to the formation of (localized) coherent CCIs and fcc Cu–Zr solid solution; while above this critical size RID leads to the formation of (localized) incoherent CCIs and Cu<sub>10</sub>Zr<sub>7</sub> intermetallics.

ANLs. The average diameter of He bubbles ( $d_{bub}$ ) in Cu layers was determined by relating the measured length and the corresponding defocus condition, following the method adopted by Wei et al. [17] and by Li et al. [14], and was summarized in Table 1. It is found that when  $h$  decreases from 150 to 2.5 nm the determined bubble spacing ( $l_{bub}$ ) [17] increases from  $\sim 4.5 \pm 0.35$  to  $\sim 8.5 \pm 0.5$  nm whereas the He-bubble density ( $N_{bub} \approx \frac{1}{l_{bub}^2 d_{bub}}$ ) of Cu layers is remarkably decreased by  $\sim 4$  times with decreasing  $h$ . In addition, the bubble diameter is almost the same ( $d_{bub}$ ,  $2.3 \pm 0.25$  nm) in all the Cu/Cu–Zr C/ANLs, regardless of layer thickness  $h$ . The increased  $l_{bub}$  and reduced  $N_{bub}$  with decreasing  $h$  are reasonable, because interfaces can serve as effective sinks by trapping or absorbing and annihilating radiation-induced defects [6,14] and He atoms [43,44]. Reducing  $h$  (increasing the interface number) will result in the decrease of bubble density, thereby enhancing  $l_{bub}$ . These findings suggest that smaller  $h$  C/ANLs exhibit greater radiation tolerance [13–17,19,20].

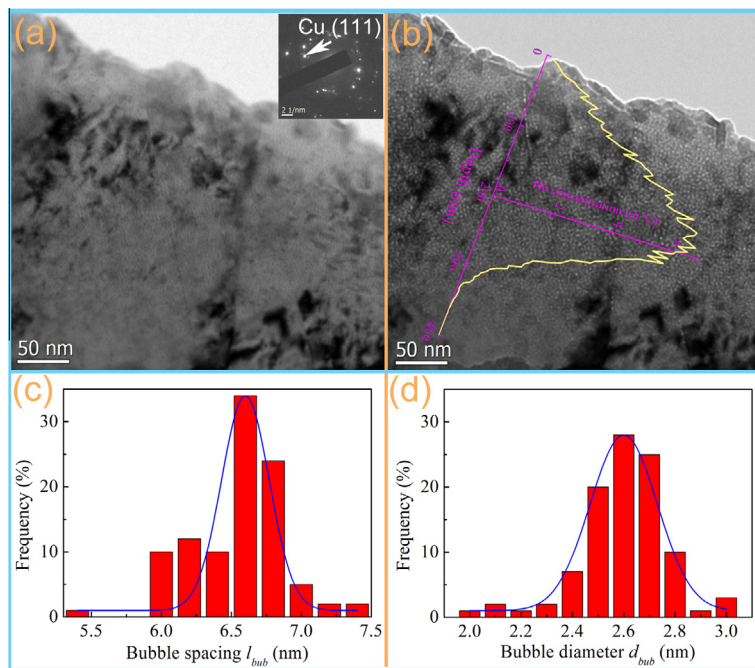


**Fig. 6.** Bubble morphology for Cu thin films after radiation. (a) Under-focus of 0 nm ( $\Delta f = 0$  nm). (b) Bubbles become white dots when under-focus of 500 nm ( $\Delta f = -500$  nm). Superimposed on image (b) is the He concentration vs. Depth profile simulated by SRIM. Bubble spacing  $l_{bub}$  (c) and bubble diameter  $d_{bub}$  (d) histograms for He-irradiated Cu thin film. Lines are visual guides.

**Table 1.** Experimental measurement on parameters of bubbles in He-irradiated Cu/Cu–Zr C/ANLs at different  $h$  and hardness of Cu/Cu–Zr at different  $h$  before and after radiation.

Sample $h$ /nm	Bubbles in Cu layers			Before radiation	After radiation	Difference
	$d_{bub}$ /nm	$l_{bub}$ /nm	$N_{bub}/10^{-3} \text{ nm}^{-3}$	Hardness $H$ /GPa	Hardness $H$ /GPa	$\Delta H$ /GPa
2.5	$2.30 \pm 0.31$	$8.50 \pm 0.51$	6.01	$6.46 \pm 0.15$	$6.56 \pm 0.21$	0.11
5	$2.40 \pm 0.25$	$7.92 \pm 0.36$	6.68	$6.43 \pm 0.22$	$6.61 \pm 0.20$	0.18
10	$2.16 \pm 0.22$	$7.20 \pm 0.52$	8.93	$6.10 \pm 0.12$	$6.52 \pm 0.16$	0.42
20	$2.43 \pm 0.24$	$6.93 \pm 0.60$	8.57	$5.28 \pm 0.11$	$5.88 \pm 0.06$	0.60
50	$2.64 \pm 0.41$	$6.43 \pm 0.90$	9.16	$4.93 \pm 0.16$	$5.81 \pm 0.17$	0.89
100	$2.03 \pm 0.19$	$4.97 \pm 0.42$	19.9	$4.55 \pm 0.18$	$5.78 \pm 0.12$	1.23
150	$2.28 \pm 0.20$	$4.50 \pm 0.35$	21.7	$4.46 \pm 0.16$	$5.81 \pm 0.17$	1.35

Note that the average diameter of He bubbles has little dependence on radiation depth for various irradiated Cu/Cu–Zr C/ANLs. In contrast, though some bubbles are observed at the CAIs there is no clear trend for both diameter and spacing of the bubbles. This is likely caused by the unique properties of CAIs and amorphous nature of glassy nanolayers. Our further TEM observations revealed that the maximum bubble density at 150–200 nm listed in Table 1 is about 1.5–2.4 folds of that at a depth of  $\sim 300$  nm (not shown here), as is consistent with other findings in C/CNLs [19,20]. Compared with the Cu/Cu–Zr C/ANLs, the diameter and spacing of He-bubble in irradiated Cu thin films are  $d_{bub} = 2.6 \pm 0.25$  nm and  $l_{bub} \sim 6.6 \pm 0.45$  nm, respectively (see Fig. 6). Correspondingly, the bubble density  $N_{bub}$  in Cu thin film is  $\sim 8.8 \times 10^{18} \text{ cm}^{-3}$ .

### 3.2. Size-dependent hardness of the Cu/Cu–Zr C/ANLs before and after irradiation

In our previous work, we have clearly demonstrated that there is no indentation size as well as substrate effect in the depth-range spanning from  $\sim 100$  to 300 nm for the as-deposited Cu/Cu–Zr C/ANLs [33,34]. The present indentation experiments by changing the maximum load and correspondingly changing the numbers of crossed interfaces or indentation depth ( $\sim 100$ , 200 and 300 nm), also found no apparent change in the determined hardness of the irradiated Cu/Cu–Zr C/ANLs. This finding likely suggests that there is a small rather than steep bubble gradient, as verified by our further TEM observations and others [19,20]. Theoretically, the bubble gradient effects indeed exist and render different degrees of bubble hardening, nevertheless, the relatively smaller bubble hardening caused by lower bubble density is likely compensated by the other factors, such as strain hardening of Cu layers and surface roughness. Therefore, for simplicity this bubble gradient effect on the mechanical properties was neglected in the present study, and we only focus the hardness measured at a depth of  $\sim 200$  nm, as presented in Fig. 7a for both Cu/Cu–Zr C/ANLs and Cu thin films. It appears that the hardness of as-deposited Cu/Cu–Zr C/ANLs sharply increases with decreasing  $h$  to 10 nm, below which the hardness seems to reach a plateau of  $\sim 6.45$  GPa, approaching the hardness of as-deposited amorphous Cu–Zr film, see Fig. 7a. The trend of “smaller is stronger” in the as-deposited Cu/Cu–Zr C/ANLs is consistent with the general results of other multilayer systems [33,45,46]. In contrast, it is interesting to find that the He-irradiated samples show the saturation hardness  $\sim 6.6$  GPa at small  $h < 10$  nm, above which another hardness plateau  $\sim 5.9$  GPa emerges (also see Fig. 7a). Meanwhile, as seen from Fig. 7b that the increase in hardness after radiation is gradually reduced with decreasing  $h$ , implying the suppression of radiation-induced hardening with decreasing  $h$  [13–17,19,20]. Similar phenomena have been observed in metallic C/CNLs, such as Cu/V [15], V/Ag [17], Ag/Ni [20] and Fe/W [21], as shown in Fig. 8.

### 3.3. Size-dependent SRS of the Cu/Cu–Zr C/ANLs before and after irradiation

To investigate the rate-controlling deformation mechanisms, SRS  $m$  and activation volume  $V^*$  of Cu/Cu–Zr C/

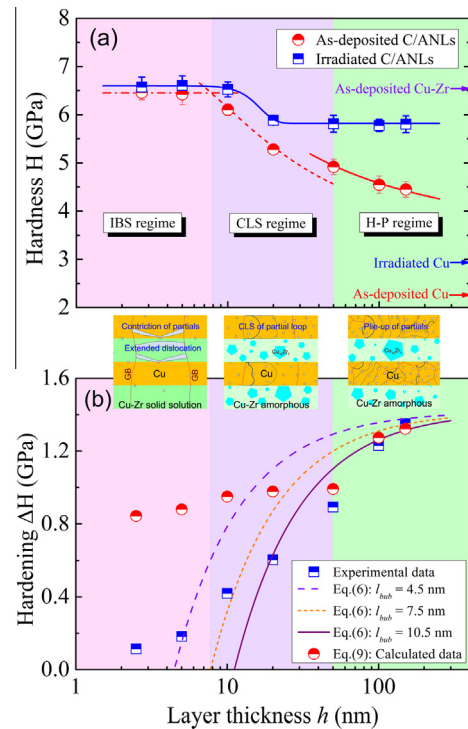


**Fig. 7.** (a) Nanoindentation hardness of the Cu/Cu–Zr C/ANLs as a function of  $h$  before and after ion-implantation. Calculations (see the red solid, dash, and dash dot lines) for the as-deposited C/ANLs from different models are plotted in the figure, divided into three regimes: IBS regime, CLS regime and H–P regime. The blue solid line is a visual guide. Hardness of Cu and Cu–Zr monolithic thin films with thickness of  $\sim 1.6 \mu\text{m}$  is also marked by arrows. (b) The size  $h$ -dependent bubble hardening in Cu/Cu–Zr C/ANLs, showing the smaller the  $h$ , the less the radiation hardening. The bubble hardening predicted from Eq. (6) at different bubble spacing is also plotted, showing a broad agreement with the experimental data; while the calculated hardening based on Eq. (9), showing great deviation from the experimental values at smaller  $h$  and well consistency at larger  $h$ . The corresponding hardening mechanisms in different length-regimes are also schematically shown in (b). For details see the text. (For interpretation of the references to color in this figure legend, the reader is referred to the web version of this article.)

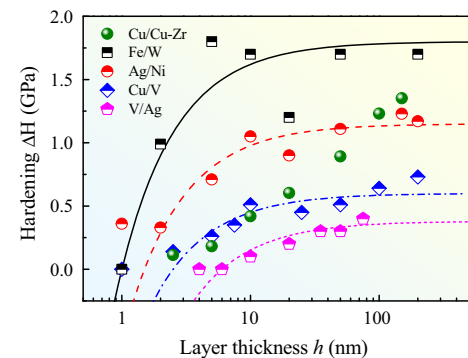


**Fig. 8.** A comparison of the size-dependent radiation hardening between the present Cu/Cu–Zr C/ANLs and reported C/CNLs, including Cu/V [15], V/Ag [17], Ag/Ni [20] and Fe/W [21], showing the smaller the  $h$ , the less the radiation hardening. The lines are visual guides.

ANLs before and after radiation are calculated and plotted as a function of  $h$  in Fig. 9a and b, respectively. SRS  $m$  monotonically increases from  $\sim 0.015$  to  $\sim 0.05$  with decreasing  $h$  from  $\sim 150$  to  $\sim 2.5$  nm for the as-deposited C/ANLs and the corresponding  $V^*$  decreases from  $\sim 16b^3$  to  $\sim 3b^3$ . Further indentation experiments by changing the indentation depth ( $\sim 100$ ,  $300$  nm), found no evident change in the determined SRS  $m$  value, similar to the case of Cu/Zr and Cu/Cr C/CNLs [38]. However, in the He-irradiated C/ANLs it is surprising to find a non-monotonic evolution of  $m$  and  $V^*$  with  $h$ . That is to say, SRS  $m$  first gradually decreases with reducing  $h$  to  $\sim 50$  nm, and subsequently increases with reducing  $h$  to  $\sim 10$  nm, and finally decreases to a constant value of  $\sim 0.016$  with further reduction in  $h$ . The  $h$ -dependent  $V^*$  has exactly an opposite evolution trend. These findings suggest that more complicated rate-controlling processes or deformation mechanisms operate in the He-irradiated C/ANLs. The measured  $V^*$  for all the as-deposited and He-irradiated samples are extremely small, falling in the range of  $\sim 1b^3$  to  $\sim 20b^3$ , similar to other multilayer systems. Similar to the cases of large  $h > 50$  nm irradiated C/ANLs, the He-irradiated Cu thin films exhibit greater SRS  $m$  or smaller  $V^*$  than that of unirradiated samples. For example, the measured SRS  $m$  is  $\sim 0.021$  and  $\sim 0.045$  for the unirradiated and irradiated Cu thin films with  $d = 180$  nm, respectively. Moreover, the measured SRS  $m$  is  $\sim 0.021$  for the as-deposited Cu thin films is quite close to the reported values  $\sim 0.02$  [42]

obtained from other testing methods at a comparable grain size.

#### 4. Discussion

Based on the microstructural observations and mechanical tests, we uncover the size constraining effect on the crystalline phase formation in Cu/Cu–Zr C/ANLs under He-irradiation, highlight that smaller  $h$  C/ANLs exhibit greater radiation tolerance, and evaluate the plastic deformation characteristics, i.e.,  $H$ ,  $m$  and  $V^*$  in above section. In this section, the influence of bubbles in Cu layers on the mechanical properties and deformation mechanisms of Cu/Cu–Zr C/ANLs will be discussed and quantitatively described, focusing on the size dependence.

##### 4.1. Radiation-induced bubble-hardening

Previous results have demonstrated that as  $h$  decreases, three different regions are frequently observed in the variation of hardness of C/ANLs [33] and C/CNLs [47,48]: the first region at microns to nanoscale ( $h > 50$  nm) shows Hall–Petch (H–P) behavior based on the dislocation pile-up against the interface, the second region at nanoscale ( $50 \text{ nm} \geq h \geq 5 \text{ nm}$ ) follows the CLS mechanism involving the glide of single dislocations in isolated layers, and the third region ( $h < 5 \text{ nm}$ ) exhibits a plateau or softening of hardness relating to the interface barrier strength (IBS) mechanism considering dislocations cutting across the interface. In the present experiments, as the length scale is greater than  $50$  nm, the hardness ( $H_{\text{H-P}}$ ) of as-deposited Cu/Cu–Zr C/ANLs can be well described by H–P relationship [33,48]:

$$H_{\text{H-P}} = H_0 + Kh^{-1/2}, \quad (3)$$

where  $H_0$  is a constant  $\sim 3.7$  GPa, originating from mainly lattice friction and  $K$  is the H–P slope  $\sim 8.8 \text{ GPa} \cdot \sqrt{\text{nm}}$ . As  $h$  falls into the CLS regime ( $50 \text{ nm} \geq h \geq 5 \text{ nm}$ ), and their deformation is dominated by soft Cu in Cu/Cu–Zr C/ANLs via partials. Considering the effect of stacking fault energy (SFE) on dislocation motion, the hardness  $H_{\text{CLS}}$  is given by the phenomenological CLS model [48,49]:

$$\begin{aligned} H_{\text{CLS}} &= 2.7 \times \sigma_{\text{CLS}} = 2.7 \times M(\tau_{\text{Orowan}} + \tau_{\text{Dis}} + \tau_{\text{SF}} - \tau_{\text{Inter}}) \\ &= 2.7 \times M \left[ \frac{\mu_{\text{Cu}} b \sin \varphi}{8\pi h_{\text{Cu}}} \left( \frac{4 - \nu}{1 - \nu} \right) \ln \left( \frac{\alpha h_{\text{Cu}}}{b \sin \varphi} \right) \right. \\ &\quad \left. + \frac{\mu_{\text{Cu}} f_{\text{Cu-Zr}} \varepsilon}{MB(1 - \nu)} + \frac{\gamma_{\text{Cu}}}{b} - \frac{F}{Mh_{\text{Cu}}} \right], \quad (4) \end{aligned}$$

where the first term  $\tau_{\text{Orowan}}$  represents the stress needed to bow out an Orowan-type dislocation to propagate, the second term  $\tau_{\text{Dis}}$  represents the dislocation–dislocation interactions during CLS, the third term  $\tau_{\text{SF}}$  is the back stress due to the stacking faults behind the gliding leading partial, and fourth term  $\tau_{\text{Inter}}$  represents the interface stress contribution and the negative sign indicates that it assists the applied stress for CLS;  $M$  is the Taylor factor,  $\varphi$  is the angle between slip plane and the interface,  $\nu$  is the Poisson ratio of Cu,  $\mu_{\text{Cu}}$  is the shear modulus of Cu,  $f_{\text{Cu-Zr}} (= h_{\text{Cu-Zr}} / (h_{\text{Cu}} + h_{\text{Cu-Zr}}) = 0.5)$  is the volume fraction of Cu–Zr glassy layers,  $\alpha$  represents the core cut-off parameter,  $F$  is the characteristic interface stress of C/ANLs, which have a typical value of  $\sim 0.5$ – $1.1 \text{ Jm}^{-2}$  for CAIs [33],  $\varepsilon$  is the in-plane plastic strain and  $B$  is a strain

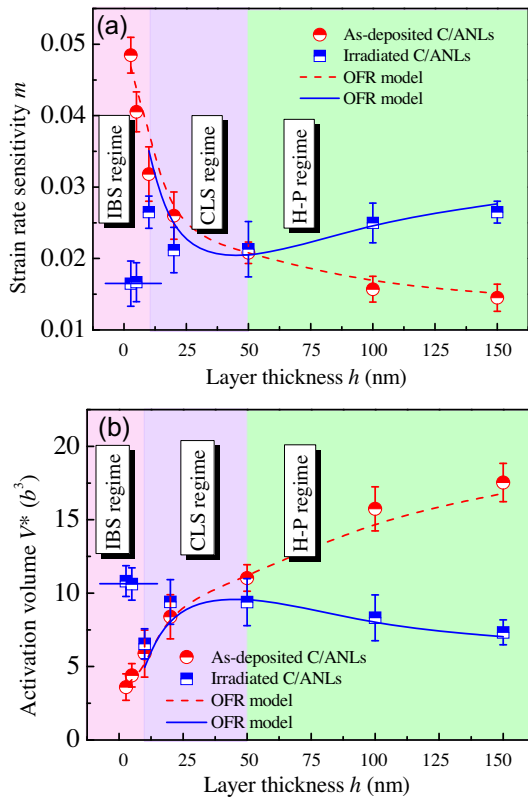


**Fig. 9.** Experimental results of strain rate sensitivity  $m$  (a), and activation volume  $V^*$  (b) as a function of  $h$  for the Cu/Cu–Zr C/ANLs before and after implantation. The solid and dashed curves in (a, b) are from the present OFR model. Three regimes, i.e., IBS regime, CLS regime and H–P regime are also marked by different colors. For details see the text. (For interpretation of the references to color in this figure legend, the reader is referred to the web version of this article.)

resolution factor of the order of 0.5 for the active slip systems. Taking  $M = 3.06$ ,  $\mu_{Cu} = 48.3$  GPa,  $\nu = 0.343$ ,  $b = 0.14757$  nm (for partials),  $\gamma_{Cu} = 0.041$  J/m<sup>2</sup>,  $\alpha = 0.15$ ,  $F = 1.1$  Jm<sup>-2</sup>,  $\varepsilon = 0.5\%$  and  $\varphi = 70.5^\circ$  into Eq. (5), the hardness of as-deposited Cu/Cu–Zr C/ANLs can be quantitatively obtained as a function of  $h$  (see the solid line in Fig. 7a), which fits the experimental results very well. However, this CLS model overestimates the hardness of  $h < 10$  nm samples, likely because the  $h$ -independent barrier to slip transmission of CAIs is reached [33,48,50]. In this length, the partials emitted from Cu layers and/or CAIs can be absorbed by glassy Cu–Zr via interface crossing mechanism [28]. The corresponding saturation hardness or IBS of C/ANLs can be approximately expressed as [51,52]:

$$H_{IBS} = 2.7 \times \sigma_{IBS} = 2.7 \times M(\tau_{Koehler} + \tau_{Partial}) \\ = 2.7 \times M \left[ \frac{\mu_A \sin \varphi}{8\pi} \left( \frac{\mu_{Cu} - \mu_A}{\mu_{Cu} + \mu_A} \right) + \frac{1}{\xi} \left( \frac{2\beta\mu_{Cu}b}{d} + \frac{\gamma_{Cu} - \gamma_A}{b} \right) \right], \quad (5)$$

where  $\sigma_{Koehler}$  is Koehler stress originating from modulus mismatch,  $\sigma_{Partial}$  is the stress needed to emit partials, including the effect of chemical interaction ( $\tau_{SEF}$ ) related to SFE difference between layer constituents (assume the SFE of amorphous Cu–Zr  $\gamma_A = 0$ ), the shear modulus of amorphous Cu–Zr layer is  $\mu_A = \frac{\mu_{Cu}\mu_{Zr}}{V_{Zr}\mu_{Cu} + V_{Cu}\mu_{Zr}} = 40.6$  GPa and can be estimated by the shear modulus  $\mu_{Cu}$  and volume fraction  $V_{Cu}$  of Cu and those of Zr,  $\beta$  reflects the characteristics of dislocations and on the order of 1,  $\xi$  is stress concentration factor of  $\sim 2$ – $4$  [52]. Taking in-plane grain size  $d = 8$  nm,  $\xi = 3$  and  $b = 0.14757$  nm, it is found that Eq. (6) can predict the saturation hardness well.

In our previous work [29,30], we uncovered that the crystallization of amorphous phase does not markedly affect the strength of Cu/Cu–Zr C/ANLs micropillars, implying that the partly crystallized Cu–Zr glassy nanolayers still sustain higher strength than the Cu nanolayers. Here, we also found that the amorphous Cu–Zr thin films before and after radiation have almost identical hardness. Hence, we reasonably assume that plastic deformation of Cu/Cu–Zr C/ANLs is dominated by soft Cu layers [47,48]. Given that the internal defect feature in irradiated Cu/Cu–Zr C/ANLs and Cu films is dominated by nanoscale He bubbles with a concentration far greater than 1 at.% [15,16,24], the radiation hardening will be interpreted in light of the pinning of glide dislocations at these bubbles. Due to the high density of bubble obstacles, the force that the obstacles exert on the dislocations is confined to a small segment of dislocations over a long bowed-out length. With increasing  $h$  from the IBS regime into the CLS regime, even into the H–P regime, the hardening ( $\Delta H$ ) due to dislocation pinning at point obstacles can be given as follows by considering the equilibrium between line force and resistance of all bubbles over the length [17]:

$$\Delta H = 2.7\Delta\sigma = 2.7M\tau_i \left( 1 - \frac{l_{bubble} \sin \varphi}{h\sqrt{\cos \varphi_c}} \right), \quad (6)$$

where  $\tau_i$  is the average shear strength of the bubble, and

$$\cos \varphi_c = \frac{\ln(\beta\bar{D}/b)}{\ln(l_{bubble}/b)} = \frac{\ln[\beta(d_{bubble}^{-1} + l_{bubble}^{-1})^{-1}/b]}{\ln(l_{bubble}/b)}, \quad (7)$$

where  $\varphi_c$  is half of a critical bow-out angle between lines of a dislocation cutting an obstacle and falls in the range of  $0$ – $\pi/2$  for weak obstacles,  $\beta$  is a coefficient of  $\sim 1$ – $4$  [17]. Using  $\tau_i = 0.17$  GPa and  $N_{bubble}$  listed in Table 1, it is found that the

increased hardness of irradiated Cu/Cu–Zr C/ANLs can be broadly captured by Eq. (6), see Fig. 8b. The obtained average obstacle strength  $\tau_i = 0.17$  GPa agrees with the reported values  $\sim 0.1$ – $0.2$  GPa [17,20,24].

According to the deformation mechanisms in as-deposited C/ANLs aforementioned before, the radiation-induced hardening behavior can thus be elucidated in three regimes at different length scales as follows:

(i) IBS regime ( $h \leq 10$  nm): As  $h$  is sufficiently small so that the interface crossing mechanism dominates in the irradiated C/ANLs, most defects (He bubbles) created by collision move into interfaces with spacing  $l_{bubble} \geq h$  and thus very few obstacles induced by implantation interfere with the crossing dislocations (see the inset in IBS regime of Fig. 7b). Compared with the as-deposited C/ANLs, the measured hardness of irradiated samples seems to suggest that the effect of interfacial He bubbles on the interface barrier to slip transmission in nanolayered fcc/fcc composites is quite small, in addition to bubble hardening. However, this should be the combining effects of He bubbles at CCIs, because the growth of bubbles at CCIs can reduce the resistant strength of interfaces on the one hand and the over-pressurized He bubbles at CCIs significantly interfere with the transmission of partials on the other hand. Consequently, these partials were required to constrict to full dislocations (in Cu) before proceeding to the adjacent fcc Cu–Zr layers. Once this full dislocation transmits across the interface, it likely recovers the original state, i.e., extended dislocation, before cutting cross next interface. Previous atomic simulations also indicated that the extended dislocation is more preferred to glide inside isolated thinner layers before it transmits across the (coherent) interface in polycrystalline nanostructured Cu/Ag multilayers [49]. Therefore, after the glassy Cu–Zr layers transformed into the fcc Cu–Zr solid solution layer, the coherent CCI barrier resistance associated with the weak obstacles (at CCIs) hardening ( $\tau_{Bubble}$ ) for slip transmission can be roughly estimated by considering the constriction stress ( $\tau_{Constriction}$ ) for two partials that combine into a full dislocation to cross the coherent CCI [19] as:

$$H_{IBS} = 2.7 \times M(\tau_{Koehler} + \delta\tau_{Koehler} + \tau_{SEF} + \tau_{Constriction} + \tau_{Bubble}) \\ = 2.7 \times M \left[ \frac{\mu_{CuZr} \sin \varphi}{8\pi} \left( \frac{\mu_{Cu} - \mu_{CuZr}}{\mu_{Cu} + \mu_{CuZr}} \right) \right. \\ \left. + \frac{\mu_{Cu}}{250} + \frac{\gamma_{Cu} - \gamma_{CuZr}}{b} + \tau_{Constriction} + \tau_{Bubble} \right], \quad (8)$$

where  $\delta\tau_{Koehler}$  is the increase in Koehler stress due to the change in elastic constants of constituents of  $\sim 0.004 \mu_{Cu}$  [50],  $\tau_{Constriction}$  is on the order of  $\sim 0.0025$ – $0.005 \mu_{Cu}$  [19] and

$$\tau_{Bubble} = \frac{1}{8} \mu_{Cu} b d_{bubble} N_{bubble}^{2/3} \approx \frac{\mu_{Cu} b}{2\pi l_{bubble}} \ln \left( \frac{2l_{bubble}}{d_{bubble} \sqrt{\cos \varphi_c}} \right) (\cos \varphi_c)^{3/2}. \quad (9)$$

Assuming  $\mu_{CuZr} = \mu_A = 40.6$  GPa,  $\gamma_{CuZr} = 0.03$  J/m<sup>2</sup> and  $\tau_{Constriction} = 0.0025 \mu_{Cu}$ , and taking  $N_{bubble}$  listed in Table 1, the calculated IBS is  $\sim 6.6$  GPa, consistently with the experimental finding well.

(ii) CLS regime ( $10 \text{ nm} < h < 50 \text{ nm}$ ): As  $h$  is larger such that, similar to the as-deposited C/ANLs, the CLS mechanism dominates in the irradiated samples, bubbles nucleate and grow at interfaces and inside layers. Bubbles inside layers act as obstacles that can enhance the hardness, leading

to radiation-induced hardening (see the inset in CLS regime of Fig. 7b).

(iii) H–P regime ( $h \geq 50$  nm): As  $h$  is quite large the dislocation pile-up mechanism that works in the as-deposited C/ANLs still dominates in the irradiated samples. It is normally anticipated that radiation-induced hardening in multilayers should be the same as that in the present pure Cu thin films via the Orowan–Frank–Read (OFR) type motion of dislocations pinned by obstacles (see the inset in Fig. 7b).

Therefore, by comparing  $l_{\text{bubble}}$  with  $h$ , one can argue that at small  $h \leq 10$  nm, the saturation hardness mainly stems from the crossing of single dislocations across interfaces containing a distribution of nanoscale He bubbles in the interface plane; whereas at large  $h > 10$  nm gliding dislocations that break away from the bubble pinning points contribute to the hardness plateau, in addition to the  $h$ -dependent strengthening effect. Actually, at large length in the H–P regime, the bubble hardening is most favorable to be interpreted in terms of the dispersed He bubbles based on Friedel–Kroupa–Hirsch model, which is given by [16,17]:  $\Delta H_{\text{H-P}} = 2.7M\tau_{\text{Bubble}}$ . Taking the experimental data, the increment in hardness of irradiated C/ANLs with  $h \geq 50$  nm can be fitted well by Eq. (9), which far overestimates the hardening at  $h < 50$  nm, see red half circles in Fig. 7b. Note that Eq. (9) can also be used to quantify the bubble hardening of  $\sim 0.76$  GPa in the present irradiated Cu films.

Finally, we compare the size-dependent radiation tolerance between the present C/ANLs and reported C/CNLs, including fcc/bcc Cu/V [15] and Ag/V [17], fcc/fcc Ag/Ni [20] and bcc/bcc Fe/W [21], to briefly elucidate the similarities/differences between these two kinds of NL material under similar He-implantation conditions. As can be seen from Fig. 8 that, as a whole, both the present C/ANLs and reported C/CNLs mentioned above manifest the similar trend that the smaller the  $h$ , the less the radiation hardening. However, it is interesting to find that Cu/Cu–Zr C/ANLs samples exhibit a sharp increase in radiation hardening with increasing  $h$  in the studied  $h$ -range. In contrast, all these C/CNLs at great  $h \geq 20$  nm show a radiation hardening plateau, whereas at small  $h < 20$  nm, fcc/bcc (Cu/V, Ag/V) C/CNLs display a gradual increase in hardening with increasing  $h$ , and fcc/fcc Ag/Ni and bcc/bcc Fe/W also exhibit an abrupt hardness increase. This radical difference between the C/ANLs and C/CNLs at large  $h \geq 20$  nm is likely caused by their different interfacial structures; namely, the former maintains CAIs with a very low bubble density while the latter possesses CCIs with a high bubble density after radiation. Apart from the interface properties, it is worth emphasizing that interfacial bubbles not only degrade the strength of the interface, also affect the dislocation activities. Additionally, it seems that the bcc/bcc Fe/W exhibits the highest radiation hardening, followed by fcc/fcc and fcc/bcc systems, at a given  $h$  within this set of limited data; however, the underlying mechanism and their interfacial radiation tolerance remain unclear and are interesting subjects. Further comparison among different C/CNL systems is ongoing and beyond the scope of this work.

#### 4.2. Intrinsic layer thickness/bubble spacing dependent SRS

Unlike the monotonically increased SRS  $m$  (and  $V^*$ ) in the as-deposited Cu/Cu–Zr C/ANLs, the irradiated samples

displayed a non-monotonic evolution in SRS  $m$  (and  $V^*$ ). Sharma et al. [53,54] have pointed out that the rate-controlling deformation mechanism in irradiated NC Ni was the interactions of dislocations with radiation-induced defects and the SRS  $m$  was enhanced with increasing radiation fluence. In our study, the suppression of radiation-induced defects with decreasing  $h$  as well as the reduced bubble-hardening signifies the more interactions of dislocations with bubbles for the irradiated Cu/Cu–Zr C/ANLs at large  $h$ . The reduced dislocation-bubble interactions with decreasing  $h$  will give rise to a decrease in SRS. On the other hand, when the numbers of interfaces increase with decreasing  $h$ , the interactions between dislocations and interfaces are enhanced, leading to an increase in SRS  $m$ . Therefore, there exists a competition between these two opposite effects that results in the non-monotonic SRS in the present He-irradiated Cu/Cu–Zr C/ANLs. In other words, the SRS is predominantly controlled by dislocation-bubble interactions at great  $h$ , whereas it is mainly controlled by dislocation-interface interactions at small  $h$ . This is consistent with the above discussion on the bubble-hardening.

Next we will quantitatively capture the size dependent SRS in Cu/Cu–Zr C/ANLs before and after radiation in the light of a thermally activated depinning process of dislocations in the form of OFR type bow-out pinned by obstacles [55] (termed as OFR model hereafter). This model [55] was proposed by Nabarro to reconcile the Cottrell–Stokes law with FRS operation, and included two components to the activation volume. The first corresponds to the classical description of the activation volume of a bowing dislocation segment between two perfectly immobile pinning points. The second component accounts for the finite strength, and thus the motion, of these pinning points. In our case, the bubbles, i.e. weak obstacles, exert finite strength of  $\sigma_{\text{Orowan}}$  and have a finite range of action (the dislocation advances rigidly across them), while the heterophase interface/boundary pinning points are approximately taken to be fixed impenetrable point barriers with infinite strength of  $\sigma_{\text{CLS}}$  (the dislocation bows out between them, and in fact, the thermally activated depinning process of a dislocation at such boundary pinning points is suggested by Swygenhoven et al. via molecular dynamics simulation [56]). Following the Nabarro's derivation, the OFR model can be respectively given by [55]

$$V^* = K_2 \left( 1 - \frac{\sigma_{\text{Orowan}}}{\sigma_{\text{CLS}}} \right)^{1/2} b l^2, \quad (10)$$

for impenetrable point barriers (layer–layer interfaces or internal obstacles in as-deposited Cu/Cu–Zr C/ANLs) and

$$V^* = K_1 \left( 1 - \frac{b l \sigma_{\text{Orowan}}}{F} \right)^{1/2} b^2 l, \quad (11)$$

for penetrable obstacles (bubbles in the present He-irradiated C/ANLs), where  $K_1$  and  $K_2$  are proportional factors,  $l$  is the obstacles spacing,  $F \approx b l (\sigma_{\text{CLS}} + \Delta\sigma)$  is the maximum force exerted by obstacles (which is somewhat greater than  $b l (\sigma_{\text{CLS}} + \Delta\sigma)$  [55]). In the as-deposited C/ANLs, however, no dispersed bubbles are present and Eq. (10) is applicable. Firstly taking  $l = h$ , one can find the calculations from Eq. (10) far overestimate  $V^*$  especially at great  $h$  (not shown here). This implies  $l$  cannot be assigned directly as  $h$ . Actually, it appears that the  $l$  should be far less than  $h$  due to polycrystalline microstructure of individual layers in the C/ANLs. In the layer thickness

direction, there are two or more grains, particularly in large  $h$  ( $>50$  nm) samples. The features of the micro/nanostructure of polycrystalline C/ANLs should be taken into account when describing the thermal activation process. Given the dislocation line tension is grain size dependent in nanocrystalline metallic materials, which can be represented by the logarithmic term in the energy per unit length of dislocations [57],

$$E_L = \frac{\mu b^2}{2} \cdot f(\lambda) = \frac{\mu b^2}{2} \cdot \frac{1 + \nu - 3\nu \sin^2 \psi}{2\pi(1 - \nu)} \ln \left( \frac{\lambda}{2b} \right), \quad (12)$$

it is assumed that the length  $\lambda$  of the dislocation segment, for which the Burgers vector  $b$  makes an angle  $\psi$  with the line vector, acts as Frank–Read (FR) source scales with the grain size. The maximum shear stress  $\tau_c$  for the bow-out segment in an equilibrium configuration is given by [57]

$$\tau_c = \frac{\mu b}{\lambda} \cdot f(\lambda). \quad (13)$$

Here in the present as-deposited C/ANLs, we similarly assume that the dislocation line tension is thickness dependent and assume the *effective* spacing of obstacles ( $l_{eff}^*$ ) exists. The *effective* spacing of obstacles,  $l_{eff}^*$ , will be estimated to calculated  $V^*$  and is given by

$$\begin{aligned} l_{eff}^* &= \frac{2.7M\mu_{Cu}b}{H} \cdot f(\lambda) \\ &= \frac{2.7M\mu_{Cu}b}{H} \cdot \frac{1 + \nu - 3\nu \sin^2 \psi}{2\pi(1 - \nu)} \ln \left( \frac{l_{eff}^*}{2b} \right). \end{aligned} \quad (14)$$

By using  $l_{eff}^*$ , calculations from Eq. (10) fit well with the experimental data of the as-deposited Cu/Cu–Zr C/ANLs, see dash line in Fig. 9b. This means that the *effective* obstacle spacing is applicable for describing the thermal activation process in the as-deposited C/ANLs.

By contrast, in the He-irradiated C/ANLs, however, the dispersed bubbles within the Cu layers and the bubbles distributed at the interfaces both have spacing smaller than the *effective* obstacle spacing, so it is reasonable to use  $l_{bub}$  in calculating  $V^*$  of the He-irradiated Cu/Cu–Zr C/ANLs by using Eq. (11) in these two regimes ( $h > 10$  nm). The calculations based on Eq. (11) can capture well the  $h$ -dependent  $V^*$  in the irradiated C/ANLs with  $l = l_{bub}$ , see the solid line in Fig. 9b. Two regimes, i.e., I-Regime (i.e., H–P regime) and II-Regime (i.e., CLS regime), are divided by the critical size of  $h \sim 50$  nm. In the H–P regime, the dislocation-bubble interactions in Cu layers is the predominant deformation mechanism, while in the CLS regime, the combination of dislocation-interface with dislocation-bubble interactions governs the plastic deformation. (Note that Eqs. (10) and (11) can also be employed to calculate  $V^*$  of pure Cu thin films before and after radiation.) With further reducing  $h$  into the IBS regime, the partial (or extended) dislocations with constant  $l_{eff}^*$  (comparable to  $l_{bub}$ ) can transfer across the interface as analyzed before [39–41]. Correspondingly, the size-independent  $V^*$  and  $m$  can be obtained, which agrees well with the data in the IBS regime, see Fig. 9b.

## 5. Conclusions

Nanostructured metallic multilayers can be designed to produce ultra-high strengths and enhanced radiation

damage tolerance via tailoring of length scales to take advantage of the atomic structure and energetic of interfaces. The radiation-induced defects have an important impact on the deformation mechanism of Cu/Cu–Zr C/ANLs. By comparing the plastic deformation characteristics of Cu/Cu–Zr C/ANLs before and after radiation, we summarized the main findings as follows.

- (1) A significant size- $h$  constraining effect on the formation of Cu–Zr phases emerges in devitrification of Cu–Zr metallic glasses under He-irradiation, i.e., at great  $h \geq 10$  nm the Cu–Zr glassy layers crystallized into the Cu<sub>10</sub>Zr<sub>7</sub> intermetallics, below which amorphous Cu–Zr crystallized into the fcc solid solution.
- (2) The radiation-induced hardness increase in Cu/Cu–Zr C/ANLs is suppressed with reducing  $h$ , and a noticeable bubble hardening exist at large  $h$  ( $h \geq 50$  nm) due to the enhanced dislocation-bubble interactions. Size-dependent radiation hardening is explained by the dislocation-bubble interaction at different length scales.
- (3) Unlike the as-deposited Cu/Cu–Zr C/ANLs, which have a monotonic size-dependent SRS and activation volume, non-monotonic variation in SRS (and activation volume) emerges in the He-irradiated C/ANLs, which is rationalized by considering the dislocation-interface interaction in terms of dislocation cutting cross the interface and dislocation-bubble interaction in terms of depinning process of dislocations in the form of OFR type bow-out.

## Acknowledgements

This work was supported by the National Natural Science Foundation of China (Grant Nos. 51201123, 51322104, 51321003), the 973 Program of China (Grant No. 2010CB631003), and the 111 Project of China (B06025). GL thanks the support from Fundamental Research Funds for the Central Universities and the Tengfei Scholar project. JYZ thanks the China Postdoctoral Science Foundation (2012M521765) and the Shaanxi Province Postdoctoral Scientific Research Projects for part of financial support.

## References

- [1] S.J. Zinkle, G.S. Was, Acta Mater. 61 (2013) 735–758.
- [2] A.K. Tyagi, R.V. Nandedkar, J. Nucl. Mater. 132 (1985) 62–69.
- [3] H. Trinkaus, B.N. Singh, S.I. Golubov, J. Nucl. Mater. (2000) 283–287, Part 1:89–98.
- [4] B.N. Singh, S.J. Zinkle, J. Nucl. Mater. 217 (1994) 161–171.
- [5] M.J. Demkowicz, R.G. Hoagland, J.P. Hirth, Phys. Rev. Lett. 100 (2008) 136102.
- [6] M.J. Demkowicz, D. Bhattacharyya, I. Usov, Y.Q. Wang, M. Nastasi, A. Misra, Appl. Phys. Lett. 97 (2010) 161903.
- [7] M.J. Demkowicz, A. Misra, A. Caro, Curr. Opin. Solid State Mater. Sci. 16 (2012) 101–108.
- [8] Z. Jiao, G.S. Was, J. Nucl. Mater. 407 (2010) 34–43.
- [9] S.J. Zinkle, J.T. Busby, Mater. Today 12 (2009) 12–19.
- [10] R.E. Baumer, M.J. Demkowicz, Acta Mater. 83 (2015) 419–430.
- [11] M.J. Demkowicz, P. Bellon, B.D. Wirth, MRS Bull. 35 (2010) 992–998.
- [12] I.J. Beyerlein, A. Caro, M.J. Demkowicz, N.A. Mara, A. Misra, B.P. Uberuaga, Mater. Today 16 (2013) 443–449.
- [13] X.-M. Bai, A.F. Voter, R.G. Hoagland, M. Nastasi, B.P. Uberuaga, Science 327 (2010) 1631–1634.

- [14] N. Li, M. Nastasi, A. Misra, *Inter. J. Plast.* 32–33 (2012) 1–16.
- [15] E.G. Fu, A. Misra, H. Wang, L. Shao, X. Zhang, *J. Nucl. Mater.* 407 (2010) 178–188.
- [16] N. Li, M.S. Martin, O. Anderoglu, A. Misra, L. Shao, H. Wang, X. Zhang, *J. Appl. Phys.* 105 (2009) 123522.
- [17] Q.M. Wei, N. Li, N. Mara, M. Nastasi, A. Misra, *Acta Mater.* 59 (2011) 6331–6340.
- [18] S. Mao, S. Shu, J. Zhou, R.S. Averback, S.J. Dillon, *Acta Mater.* 82 (2015) 328–335.
- [19] Y. Chen, Y. Liu, E.G. Fu, C. Sun, K.Y. Yu, M. Song, J. Li, Y.Q. Wang, H. Wang, X. Zhang, *Acta Mater.* 84 (2015) 393–404.
- [20] K.Y. Yu, Y. Liu, E.G. Fu, Y.Q. Wang, M.T. Myers, H. Wang, L. Shao, X. Zhang, *J. Nucl. Mater.* 440 (2013) 310–318.
- [21] N. Li, E.G. Fu, H. Wang, J.J. Carter, L. Shao, S.A. Maloy, A. Misra, X. Zhang, *J. Nucl. Mater.* 389 (2009) 233–238.
- [22] A. Hirata, P. Guan, T. Fujita, Y. Hirotsu, A. Inoue, A.R. Yavari, T. Sakurai, M. Chen, *Nat. Mater.* 10 (2010) 28–33.
- [23] H.W. Sheng, W.K. Luo, F.M. Alamgir, J.M. Bai, E. Ma, *Nature* 439 (2006) 419–425.
- [24] C.A. Schuh, T.C. Hufnagel, U. Ramamurty, *Acta Mater.* 55 (2007) 4067–4109.
- [25] Y. Watanabe, S. Nanao, A. Kohyama, *J. Nucl. Mater.* 122 (1984) 743–747.
- [26] T. Nagase, Y. Umakoshi, *Mater. Sci. Eng. A* 352 (2003) 251–260.
- [27] T. Nagase, Y. Umakoshi, *Mater. Trans.* 45 (2004) 13–23.
- [28] Y.M. Wang, J. Li, A.V. Hamza, J.T.W. Barbee, *Proc. Nat. Acad. Sci. USA* 104 (2007) 11155–11160.
- [29] J.Y. Zhang, G. Liu, J. Sun, *Acta Mater.* 66 (2014) 22–31.
- [30] J.Y. Zhang, G. Liu, J. Sun, *Sci. Rep.* 3 (2013) 2324.
- [31] J.Y. Zhang, J. Li, X.Q. Liang, G. Liu, J. Sun, *Sci. Rep.* 4 (2014) 04205.
- [32] C. Brandl, T.C. Germann, A. Misra, *Acta Mater.* 61 (2013) 3600–3611.
- [33] J.Y. Zhang, Y. Liu, J. Chen, Y. Chen, G. Liu, X. Zhang, *J. Sun, Mater. Sci. Eng. A* 552 (2012) 392–398.
- [34] J.Y. Zhang, G. Liu, S.Y. Lei, J.J. Niu, J. Sun, *Acta Mater.* 60 (2012) 7183–7196.
- [35] K. Hattar, M.J. Demkowicz, A. Misra, I.M. Robertson, R.G. Hoagland, *Scr. Mater.* 58 (2008) 541–544.
- [36] R.F. Egerton, *Electron Energy Loss Spectroscopy in the Electron Microscope*, Springer, Berlin, 2011.
- [37] W.C. Oliver, G.M. Pharr, *J. Mater. Res.* 7 (1992) 1564–1583.
- [38] J.J. Niu, J.Y. Zhang, G. Liu, P. Zhang, S.Y. Lei, G.J. Zhang, J. Sun, *Acta Mater.* 60 (2012) 3677–3689.
- [39] P. Huang, F. Wang, M. Xu, K.W. Xu, T.J. Lu, *Acta Mater.* 58 (2010) 5196–5205.
- [40] Z.H. Cao, L. Wang, K. Hu, Y.L. Huang, X.K. Meng, *Acta Mater.* 60 (2012) 6742–6754.
- [41] R. Goodall, T.W. Clyne, *Acta Mater.* 54 (2006) 5489–5499.
- [42] J. Chen, L. Lu, K. Lu, *Scr. Mater.* 54 (2006) 1913–1918.
- [43] A. Kashinath, A. Misra, M.J. Demkowicz, *Phys. Rev. Lett.* 110 (2013) 086101.
- [44] N. Li, J.J. Carter, A. Misra, L. Shao, H. Wang, X. Zhang, *Philos. Mag. Lett.* 91 (2011) 18–28.
- [45] J.Y. Zhang, J.J. Niu, X. Zhang, P. Zhang, G. Liu, G.J. Zhang, *J. Sun, Mater. Sci. Eng. A* 543 (2012) 139–144.
- [46] A. Misra, M. Verdier, Y.C. Lu, H. Kung, T.E. Mitchell, M. Nastasi, J.D. Embury, *Scr. Mater.* 39 (1998) 555–560.
- [47] J.Y. Zhang, S.Y. Lei, Y. Liu, J.J. Niu, Y. Chen, G. Liu, X. Zhang, *J. Sun, Acta Mater.* 60 (2012) 1610–1622.
- [48] A. Misra, J.P. Hirth, R.G. Hoagland, *Acta Mater.* 53 (2005) 4817–4824.
- [49] Y. Zhu, Z. Li, M. Huang, *J. Appl. Phys.* 115 (2014) 233508.
- [50] Y. Liu, D. Bufford, H. Wang, C. Sun, X. Zhang, *Acta Mater.* 59 (2011) 1924–1933.
- [51] J.S. Koehler, *Phys. Rev. B* 2 (1970) 547–551.
- [52] J.Y. Zhang, X. Zhang, G. Liu, R.H. Wang, G.J. Zhang, *J. Sun, Mater. Sci. Eng. A* 528 (2011) 7774–7780.
- [53] G. Sharma, A. Sarkar, J. Varshney, U. Ramamurty, A. Kumar, S.K. Gupta, J.K. Chakravarty, *Scripta Mater.* 65 (2011) 727–730.
- [54] G. Sharma, P. Mukherjee, A. Chatterjee, *Acta Mater.* 61 (2013) 3257–3266.
- [55] F.R.N. Nabarro, *Acta Metall. Mater.* 38 (1990) 161–164.
- [56] H. Van Swygenhoven, P. Derlet, A. Froseth, *Acta Mater.* 54 (2006) 1975–1983.
- [57] A.S. Argon, *Strengthening Mechanisms in Crystal Plasticity*, Oxford University Press Inc., New York, 2008.